Ultrasound in Med. & Biol., Vol. 43, No. 9, pp. 1953–1962, 2017

0301-5629/$ - see front matter

http://dx.doi.org/10.1016/j.ultrasmedbio.2017.04.021

● *Original Contribution*

DELINEATION OF POST-PROCEDURE ABLATION REGIONS WITH ELECTRODE DISPLACEMENT ELASTOGRAPHY WITH A COMPARISON TO ACOUSTIC RADIATION FORCE IMPULSE IMAGING

WENJUN YANG,* TOMY VARGHESE,* TIMOTHY ZIEMLEWICZ,† MARCI ALEXANDER,† MEGHAN LUBNER,† JAMES LOUIS HINSHAW,† SHANE WELLS,† and FRED T. LEE, JR.†

*Department of Medical Physics, University of Wisconsin School of Medicine and Public Health, University of Wisconsin—Madison, Madison, Wisconsin, USA; and †Department of Radiology, University of Wisconsin School of Medicine and Public Health, University of Wisconsin—Madison, Madison, Wisconsin, USA

(*Received* 2 *November* 2016; *revised* 12 *April* 2017; *in final form* 20 *April* 2017)

Abstract—We compared a quasi-static ultrasound elastography technique, referred to as electrode displacement elastography (EDE), with acoustic radiation force impulse imaging (ARFI) for monitoring microwave ablation (MWA) procedures on patients diagnosed with liver neoplasms. Forty-nine patients recruited to this study underwent EDE and ARFI with a Siemens Acuson S2000 system after an MWA procedure. On the basis of visualization results from two observers, the ablated region in ARFI images was recognizable on 20 patients on average in conjunction with B-mode imaging, whereas delineable ablation boundaries could be generated on 4 patients on average. With EDE, the ablated region was delineable on 40 patients on average, with less imaging depth dependence. Study of tissue-mimicking phantoms revealed that the ablation region dimensions measured on EDE and ARFI images were within 8%, whereas the image contrast and contrast-to-noise ratio with EDE was two to three times higher than that obtained with ARFI. This study indicated that EDE provided improved monitoring results for minimally invasive MWA in clinical procedures for liver cancer and metastases. (E-mail: wyang37@wisc.edu) **© 2017 World Federation for Ultrasound in Medicine & Biology.**

Key Words: **Microwave ablation, Electrode displacement elastography, Acoustic radiation force impulse imaging, Liver cancer.**

INTRODUCTION

Microwave ablation (MWA) is a minimally invasive treatment modality used for thermal necrosis of liver tumors (Murakami et al. 1995). MWA can be performed with multiple antennas simultaneously to cover larger treated volumes, with additional benefits such as an improved heating rate while avoiding the risk of skin burns caused by the grounding pad in radiofrequency ablation (RFA) procedures (Harari et al. 2016; Liang and Wang 2007; Lubner et al. 2013; Qian et al. 2012; Wells et al. 2015; Ziemlewicz et al. 2016). Promising treatment outcomes were reported for solitary tumors less than 2 cm in diameter (Lencioni and Crocetti 2012; Shiina et al. 2012), and more recent studies indicate that MWA is successful in treating tumors larger than 3 cm (Thamtorawat et al. 2016; Ziemlewicz et al. 2015, 2016). The key factor contributing to a successful MWA procedure is the generation of a sufficient ablation margin covering the entire targeted volume (Liang and Wang 2007; Maluccio and Covey 2012). Thus, effective monitoring of the location and dimensions of the ablated region is crucial. The most widely used clinical monitoring approach for liver ablation procedures is contrast-enhanced computed tomography (CT) because of the relatively fast imaging speed and ablation equipment compatibility compared with magnetic resonance imaging (MRI). However, CT scans expose both the patient and the clinician to ionizing radiation, require use of intra-venous contrast and generally result in longer treatment durations and higher cost.

Ultrasound, the most cost-efficient and portable imaging modality, is often used to guide the insertion of the MWA antenna into the tumor (Lubner et al. 2013; Wells et al. 2015; Ziemlewicz et al. 2016). The ablated tumor

Address correspondence to: Wenjun Yang, Department of Medical Physics, University of Wisconsin School of Medicine and Public Health, University of Wisconsin—Madison, Madison, WI 53706, USA. E-mail: wyang37@wisc.edu

region can be visualized on conventional ultrasound B-mode images from the hyper-echoic region generated from the outgassing of the water vapor bubble cloud during the procedure. However, a delineable ablation zone boundary is not always achievable, particularly on the distal side of the ablation zone, because of the increased attenuation caused by the bubble cloud during the ablation procedure and the similar echogenicity between the ablated region and surrounding liver tissue after the procedure (Bharat et al. 2008b; Rubert et al. 2010; Varghese et al. 2002; Yang et al. 2016).

Shear modulus, which denotes the local stiffness of tissue, varies significantly between the ablated region and surrounding normal tissue (Sarvazyan et al. 1998). Thermal ablation causes tissue protein denaturation, inducing an increase in the shear modulus or stiffness in the ablated region (Varghese et al. 2003a, 2004). These changes appear as regions that incur less strain on deformation than surrounding untreated tissue (Varghese et al. 2002, 2003a, 2004). With strain and modulus imaging, ablated regions exhibit high contrast with respect to the normal, untreated background liver tissue. Because strain and modulus imaging can be performed during (Varghese et al. 2004) or immediately after the ablation procedure (Jiang et al. 2010; Rubert et al. 2010), complete monitoring of ablation, from guidance to preliminary follow-up, is possible using ultrasound (Zhou et al. 2014). Ultrasound elastography for ablation monitoring was initially developed using methods based on external compression (Ophir et al. 1991; Van Vledder et al. 2010) or physiologic deformation (Varghese and Shi 2004; Varghese et al. 2003b).

To overcome the limitation of external compression apparatus in clinical application, we introduced an ultrasound elastography technique referred to as electrode displacement elastography (EDE), which was designed specifically for RFA or MWA monitoring (Bharat and Varghese 2006; Bharat et al. 2008a, 2008b; Jiang et al. 2010; Rubert et al. 2010; Varghese et al. 2002; Yang et al. 2016). EDE uses minute manual perturbations of the ablation needle (Jiang et al. 2010; Rubert et al. 2010) by clinicians to introduce tissue deformations internally at the ablation site. We have reported its feasibility in both *ex vivo* (Bharat et al. 2005, 2008a; Pareek et al. 2006) and *in vivo* (Jiang et al. 2010; Rubert et al. 2010) experiments using porcine models and in human patients (Yang et al. 2016).

In this study, we compare the MWA monitoring performance of EDE with that of a commercially implemented ultrasound elastography technique, referred to as acoustic radiation force impulse (ARFI) imaging (Nightingale et al. 2001). ARFI produces stiffness images of local tissue by applying ultrasound push beams with acoustic intensities and durations significantly higher than those in diagnostic imaging to deform the local tissue, and then using beams with diagnostic intensity to analyze the local tissue displacement along the direction of the push beams. With the advantage of local compression using the push beams and decreased inter-operator variability, ARFI has been used for breast cancer detection (Nightingale et al. 2001) and RFA monitoring (Fahey et al. 2008). However, to the best of our knowledge, there are no existing literature reports on MWA monitoring using ARFI on liver neoplasms in a significant number of clinical cases.

We previously reported that the ablated region is close to an ellipsoidal shape in EDE images with enhanced signal- and contrast-to-noise ratios (SNR_e and CNR_e) compared with conventional B-mode images (Yang et al. 2016). In this study, we compared the delineation performance of EDE and ARFI on both tissue-mimicking (TM) phantoms and a clinical application for monitoring MWA ablation procedures. Phantom inclusion dimensions, image contrast and CNR_e were compared for the phantom study, followed by a binary evaluation of the delineation of the ablated region for 49 patients with liver cancer in a clinical study.

METHODS

Tissue-mimicking phantom

Two TM phantoms previously constructed using an oil-in-gelatin matrix with a stiffer partially ablated inclusion (mimicking a partially ablated tumor) (Ingle and Varghese 2014) were scanned using both ARFI and EDE. The centers of the inclusions in the two phantoms were located at depths of 3.5 and 5.5 cm, respectively. The Young's modulus contrast of the stiff ellipsoidal inclusion (mimicking the ablated region), irregularly shaped target (mimicking tumor) and background was 1.9:1.2:1, measured using a Supersonic Imagine (Supersonic, Aix-en-Provence, France) system. The three distinct regions can be distinguished on B-mode images by the different and distinct backscatter levels that were incorporated into the TM phantom manufacture, as illustrated in Figure 1(a,d). A stainless-steel needle was bonded to the inclusion to mimic the MWA antenna.

In Figure 1(b,e and c,f) are EDE and ARFI images of the TM phantom, respectively. Image contrast and contrast-to-noise ratio (CNR_e) were used to quantify the visibility of the inclusion on EDE and ARFI images. Two rectangular regions of interest (ROIs) with dimensions of 10 × 10 mm were placed inside and above the inclusion to calculate the image contrast and CNR_e using the equation

$$\text{Image contrast} = \left|\frac{I_b - I_o}{I_o + I_b}\right| \quad (1)$$

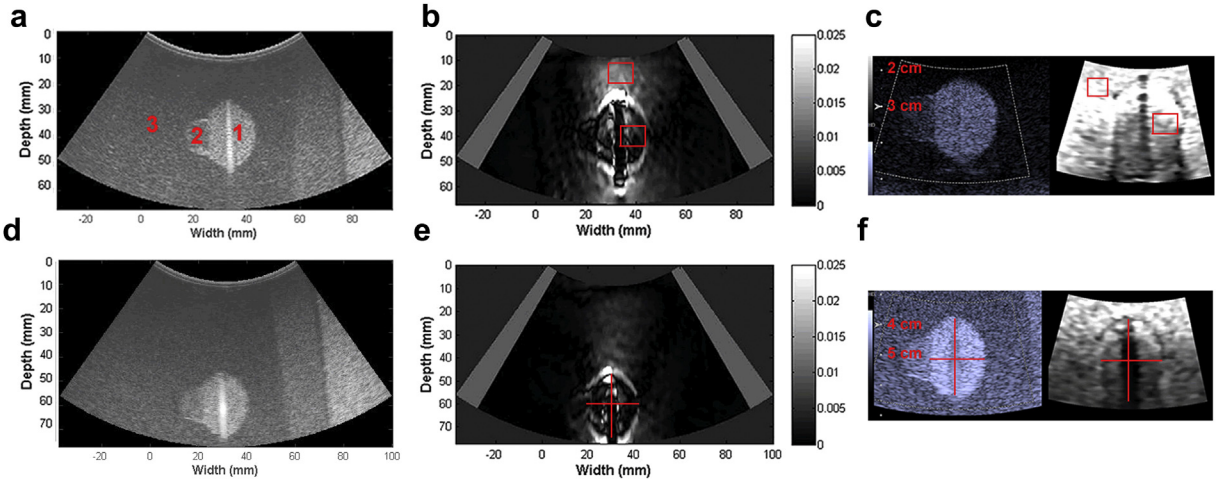

Fig. 1. B-Mode, electrode displacement elastography (EDE) and acoustic radiation force impulse (ARFI) images of the corresponding tissue-mimicking phantoms. (a–c) Phantom with inclusion at a 3.5-cm depth. (d–f) Phantom with a deeper inclusion at 5.5 cm. In the three columns are B-mode (reconstructed from radiofrequency data), EDE and ARFI images for the two phantoms, respectively. The bright regions on the right side of (a) and (d) are caused by the phantom container because of the wide field of view of the curvilinear transducer. The gray areas at the boarder of the sector images in (b) and (e) are dummy A-lines to preserve the original physical dimension. Numbers 1–3 in (a) denote the inclusion, irregularly shaped target and background, respectively. All images were acquired with a Siemens Acuson S2000 system and 6 C1 HD transducer operating at a center frequency of 4 MHz. The unit on the color bar for the strain images is strain as a percentage of the applied deformation (e.g., 0.01 corresponds to a 1% strain).

where I_b and I_o denote the mean pixel values of the ROIs placed in the background and object (inclusion), respectively. For EDE images, as illustrated in Figure 1(b), one ROI was placed in the inclusion slightly off-center to reduce strain artifacts caused by the needle, and the other ROI was placed as close as possible to the inclusion above the saturated halo to avoid decorrelation tracking noise (Bharat et al. 2008b). For ARFI images, as illustrated in Figure 1(c), the ROI inside the inclusion was placed similarly off-center of the inclusion, whereas the other ROI was placed in the upper background which was above the irregular shaped region. CNR_e was calculated using the equation

$$CNR_e = \frac{|I_o - I_b|}{\sqrt{\sigma_o^2 + \sigma_b^2}} \quad (2)$$

where I_b and I_o are the mean values as defined above, and σ_b and σ_o are the standard deviations of the ROIs placed in the background and the object (inclusion), respectively. CNR_e denotes the detectability of the inclusion taking into account the effect of noise.

Dimensions of the inclusion on EDE and ARFI images were used to compare precision of delineation between these two modalities. As illustrated in Figure 1(e,f), the long and short axes of the inclusion were measured on EDE and ARFI images, respectively. For EDE images, these dimensions were measured on strain images, as illustrated in Figure 1(e), whereas for ARFI and B-mode images, they were measured using the distance measurement built into the ultrasound system. The short axis of the inclusion was measured without the irregularly shaped region because this region cannot be visualized on ARFI images, as illustrated in Figure 1(f). The contrast, CNR_e, and inclusion dimensions were all determined from 10 independent experiments with EDE and ARFI, respectively.

Patients and MWA procedure

Forty-nine patients diagnosed with hepatocellular carcinoma (HCC), adenoma, or liver metastases and treated with a MWA procedure were recruited into our study, with both EDE and ARFI imaging performed for each patient. This study was conducted under a protocol approved by the institutional review board of the University of Wisconsin—Madison, with informed consent obtained for each patient. Patient demographic characteristics included 35 male and 14 female patients, who ranged in age from 33 to 87. Detailed demographic characteristics of the patients recruited to this study are outlined in Table 1.

Microwave ablation was performed on patients under general anesthesia, with patients placed in a supine, lateral or prone position on a CT imaging table, depending on the location of the liver tumors. MWA was performed using a Certus 140 system (Neuwave Medical, Madison, WI, USA). Single or multiple antennas were

Table 1. Patient demographics

Age (y)	
Range	33–87
Mean ± SD	62.0 ± 11.9
Gender (M/F)	35/14
Tumor type (HCC/adenoma/metastases)	37/2/10
Tumor size (mean ± SD)	2.3 ± 0.9
Cirrhosis (yes/no)	33/16
Fatty liver (yes/no)	1/49
Prior treatment (yes/no)	12/37

HCC = hepatocellular carcinoma; SD = standard deviation.

inserted based on the tumor dimensions and location, under ultrasound B-mode imaging guidance. Typical ablation power and duration were 65 W and 5 min, respectively.

EDE and ARFI data acquisition

Both ARFI and EDE studies were performed using a Siemens Acuson S2000 system (Siemens Medical Solutions, Mountain View, CA, USA) with a 6 C1 HD curvilinear transducer. For the phantom study, EDE and ARFI images were acquired at imaging depths of 6 and 7 cm, with a focus set at 3.5 or 5.5 cm, respectively, for the two phantoms, using a center frequency of 4 MHz. ARFI images were obtained using Virtual Touch software, and images were generated in real time. EDE strain images were obtained from a continuous loop of in-phase/quadrature data acquired during manual perturbation of the ablation antenna, with an amplitude of 1–2 mm. EDE strain images were computed between two in-phase/quadrature frames within the loop using a 2-D cross-correlation algorithm (Chen et al. 2009). These two frames of in-phase/quadrature data were selected manually by observing the movement of the ablation region in the B-mode images. The cross-correlation kernel dimension was selected as 0.45 × 1.41 mm to generate strain images with high SNR (Varghese 2009; Varghese and Ophir 1997). Because the A-lines with curvilinear transducers are sparser toward the bottom of the image, the tracking and processing kernel width expands accordingly with depth (Yang et al. 2016).

For the clinical study, EDE and ARFI images were sequentially acquired immediately after the MWA procedure. Imaging depth was selected to span the entire ablated region, with the focus selected to lie slightly below the ablation zone to reduce shadowing from gas bubbles generated during the ablation procedure. ARFI and EDE image acquisition protocols were similar to that used for the phantom study, and manual perturbation of the ablation needle was performed by a physician. The displacement of the MWA antenna was performed manually by the clinician in a sinusoidal manner along the axis of the antenna. Out-of-plane displacement of the antenna was minimized. For patients for whom multiple antennas were placed, only the central antenna was perturbed to obtain the EDE strain image. For patients with multiple tumors, only the first treated tumor was analyzed in this study to avoid artifacts caused by repositioning of the antennas. The 2-D cross-correlation kernel dimension used for the clinical study was 1.35 × 3.29 mm, which was larger than that used for the phantom study to include more echo signal to improve deformation tracking caused by the increased attenuation present in clinical data sets (Varghese 2009; Varghese and Ophir 1997; Yang et al. 2016). The monitoring ability of EDE and ARFI was assessed based on whether a visible boundary could be delineated to differentiate the ablated zone from the surrounding untreated tissue. In some ARFI images, the location of ablated region could be reasonably recognized with reference to the B-mode images, even though they were depicted without a clear boundary. For these cases, the monitoring ability of ARFI is defined as recognizable, which is inferior to the definition of delineable. Image analysis and reporting of the success rate for monitoring MWA using EDE and ARFI were performed by two observers based on the criteria described above. The observers include a graduate student (observer 1) with more than 4 y of experience in the processing, visualization and analysis of strain images, and a physician (observer 2) with more than 10 y of experience with MWA procedures.

RESULTS

In Figure 1(b,c and e,f) are the EDE and ARFI images of the TM phantoms. The inclusion in the EDE images of the TM phantom was identified from the background by a saturated bright halo surrounding a low-strain or darker region. In the ARFI images, the inclusions can be reasonably differentiated from the background by a dark boundary with a relatively increased noise level. The irregularly shaped target marked by the number 2, as illustrated in Figure 1(a), could be identified in EDE images (Fig. 1b,e), whereas it is not visible in ARFI images (Fig. 1c,f).

Ten independent EDE and ARFI images were acquired for both TM phantoms. The image contrast and CNR_e of the phantom with the inclusion at 3.5 cm were 3.45 ± 0.68 and 2.82 ± 0.81, respectively, and the same quantities measured on ARFI images for the same phantom were 1.03 ± 0.13 and 0.62 ± 0.32, respectively. The image contrast and CNR_e for this phantom was two to three times higher with EDE than with ARFI images as illustrated in Figure 2 (phantom 1). For the phantom with the deeper inclusion at 5.5 cm, image contrast and CNR_e in EDE images were 3.91 ± 1.63 and 2.45 ± 1.02, respectively; in ARFI images, these two

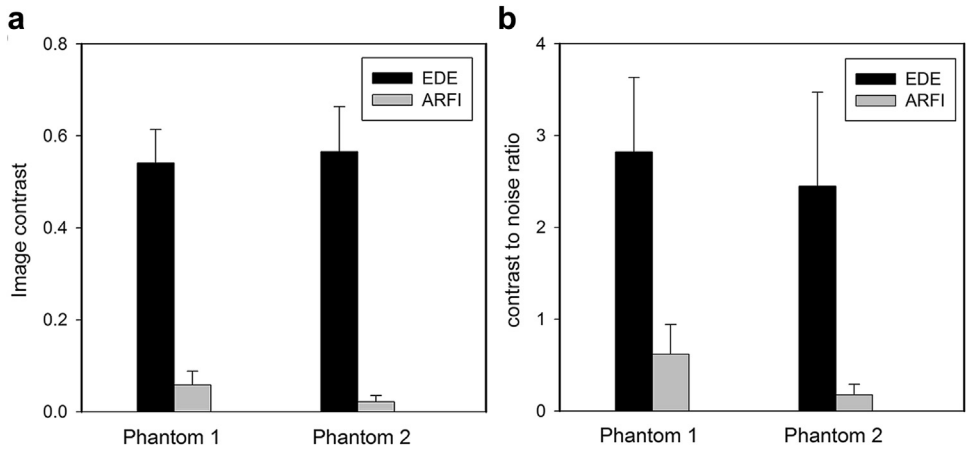

Fig. 2. Image contrast and CNR_e comparison obtained on electrode displacement elastography (EDE) and acoustic radiation force impulse (ARFI) images of tissue-mimicking phantoms. (a) Image contrast comparison of EDE and ARFI performed on the phantom with inclusion at a 3.5-cm depth (phantom 1) and at a 5.5-cm depth (phantom 2) (b) Comparison of CNR_e on the same two phantoms. The height of the bars represents the mean value of 10 independent experiments, and the error bar denotes the standard deviation of the measurements.

quantities were 1.00 ± 0.05 and 0.18 ± 0.11, respectively. The detectability of the inclusion with EDE was about 4 to 10 times higher than that with ARFI in the second phantom with a deeper inclusion, as illustrated in Figure 2 (phantom 2).

The precision of delineation in terms of inclusion dimensions for 10 independent realizations for both EDE and ARFI images is illustrated in Figure 3. The long axis (height) of the inclusion of phantom 1 was 25.67 ± 0.49, 26.21 ± 0.92 and 27.86 ± 0.92 mm measured with B mode, EDE and ARFI images, respectively, and the short axis (width) of this inclusion measured with these imaging modalities was 18.33 ± 0.26, 19.85 ± 0.20 and 19.83 ± 0.70 mm. For phantom 2, the long axis of the inclusion measured with B mode, EDE and ARFI was 25.86 ± 0.26, 26.41 ± 0.40 and 27.38 ± 0.39 mm, respectively, and the short axis measured with these three modalities was 19.43 ± 0.28, 20.70 ± 0.79 and 21.55 ± 0.35 mm, respectively. Differences in the inclusion dimensions measured with these three modalities were within 8% (2.2/25.67 ≈ 8%).

For the clinical study, results from observer 1 indicate that the liver neoplasm targeted with the MWA procedure was successfully delineated with EDE for 45 of the 49 patients. The ablated region could be delineated on two ARFI images, both presenting with tumors at depths of around 4 cm. The ablation zone with EDE was delineated by the dark region surrounded by a bright halo as illustrated in the TM phantom study. The boundary of the ablated region was relatively blurred in the ARFI images, as illustrated in Figure 4(a,d). Ablation

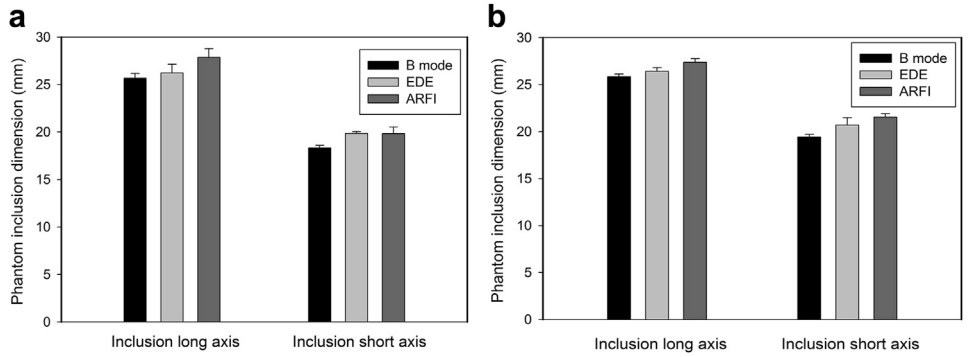

Fig. 3. Dimensions of phantom inclusion comparison among B-mode, electrode displacement elastography (EDE) and acoustic radiation force impulse (ARFI) images. (a) Long- and short-axis lengths of the phantom with inclusion at 3.5 cm (phantom 1) measured in B-mode, EDE and ARFI images. (b) Same comparison conducted for the phantom with inclusion at 5.5 cm (phantom 2). The height of the bars represents the mean value of the 10 independent imaging experiments and the error bars denote the standard deviation.

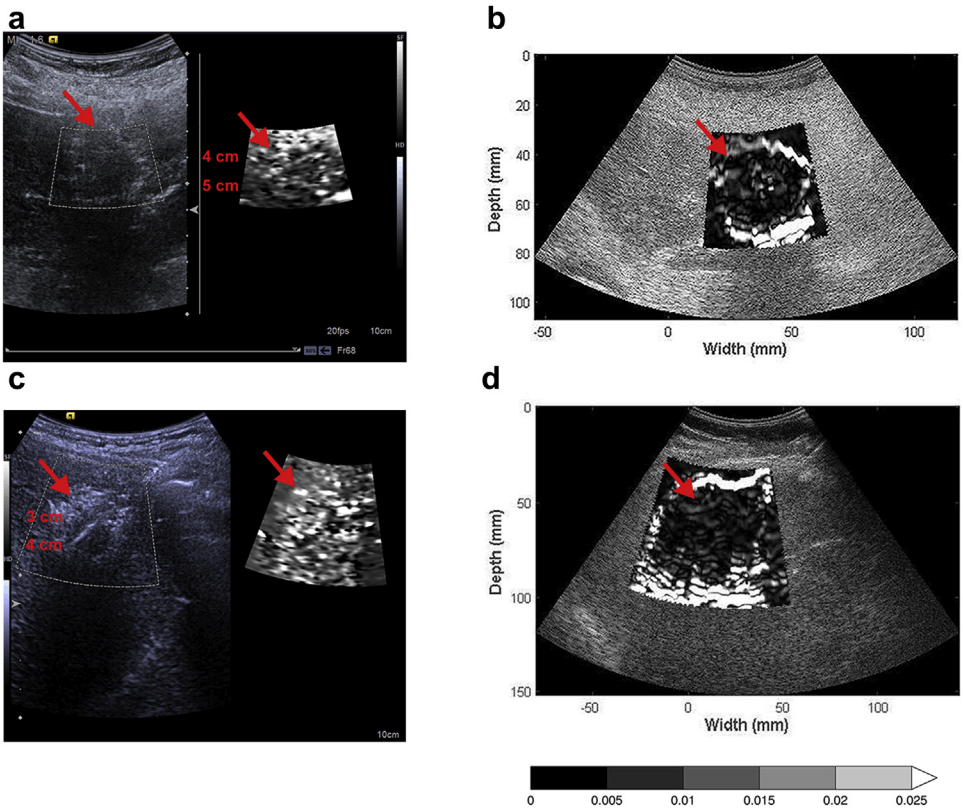

Fig. 4. Comparison of electrode displacement elastography (EDE) and acoustic radiation force impulse (ARFI) images immediately after microwave ablation. (a,c) B-Mode and ARFI images of the ablated region. (b,d) EDE images generated from radiofrequency data. The ablated region is somewhat delineable in the ARFI images (a,c).

zones were delineated using ARFI images from observer 2 for 6 of 49 patients, with 4 of the tumors at a depth lower than 5 cm, 1 tumor located between 5 and 10 cm and 1 tumor at a depth >10 cm. The number of ablation zones delineated using EDE images from observer 2 was 34.

For most of the 49 patients, the ablated region was not clearly delineable with a visible boundary as illustrated in Figure 5(a,d) for ARFI imaging. However, with reference to B-mode images, the location of the ablated region could be recognized in 13 patients with ARFI images from observer 1, as illustrated in Figure 5(d). The delineation success rate of EDE and ARFI is summarized in Table 2. It was found that the success rate decreased from 40% to 11.1% as the imaging depth increased from shallow, that is, 5 cm to deeper than 10 cm. Partially visualized ablation regions were identified on 27 patients by observer 2. The imaging depth dependence was similar to that of observer 1, dropping from 80% to 22.2% when the imaging depth increased from <5 cm to >10 cm, as outlined in Table 3.

The total success rates for boundary delineation with EDE in the 49 patients were 91.8% and 69.4%, whereas those with ARFI were 4.1% and 12.2%, respectively, for observers 1 and 2. EDE exhibited less imaging depth dependence with a relatively stable success rate for each depth range. The success rate with ARFI improved to 26.5% and 55.1%, respectively for the two observers, for partial visualization of the ablated region in conjunction with B-mode imaging. However, as tumor depth increased, the entire ablated region, especially toward the bottom of the tumor, was blurred. The numbers of delineable and partially visualized ablation regions for the two observers are illustrated in Figure 6.

DISCUSSION AND CONCLUSIONS

We have compared the performance of EDE and ARFI for monitoring minimally invasive MWA treatments for liver neoplasms in human patients along with a TM phantom study. ARFI imaging reported in this paper is based on the commercial software available on the Siemens Acuson S2000 system.

The TM phantom study revealed that both ARFI and EDE reasonably delineate a stiffer inclusion embedded in a homogeneous background. The dimensions of the inclusion in the EDE and ARFI images were in a similar range within 8% difference, although the long and short axes appeared slightly larger on ARFI images. The

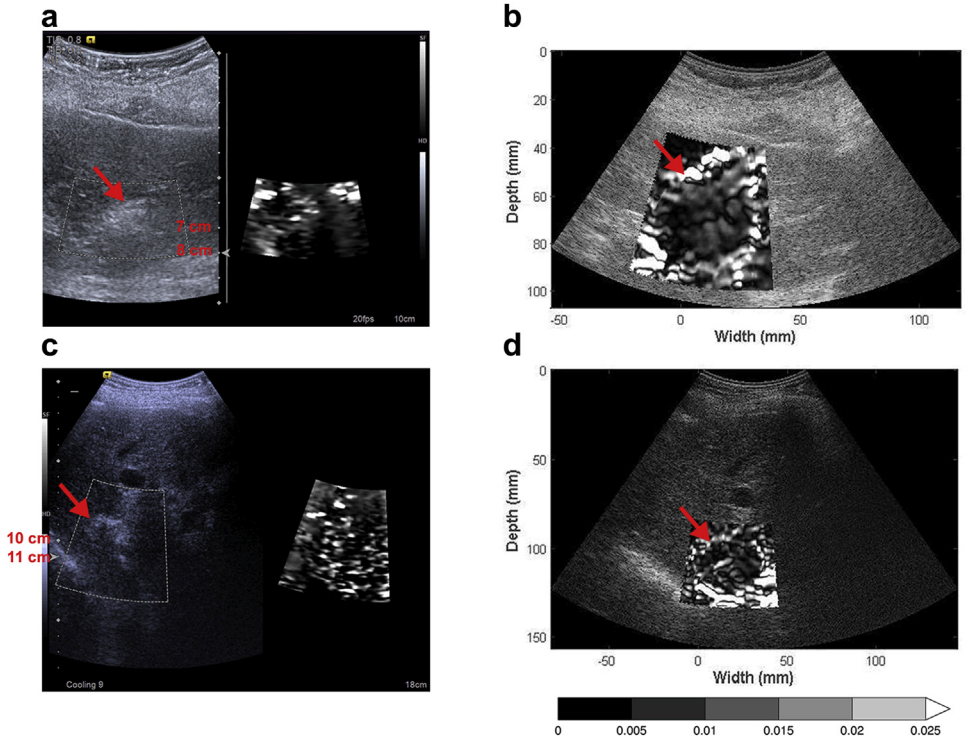

Fig. 5. Comparison of electrode displacement elastography (EDE) and acoustic radiation force impulse (ARFI) images immediately after microwave ablation (MVA). (a,c) B-Mode and ARFI images of the ablated region. (b,d) EDE images generated from radiofrequency data. The ablated region was not delineable in the ARFI images (a,c), although with reference to the B-mode image, the location of the ablated region is recognizable with a distorted shape in (c).

detectability of the inclusion was enhanced in EDE images with a two to three times higher image contrast and CNR_e and with less imaging depth dependence between the two phantoms evaluated. As illustrated in Figure 3, the image contrast and CNR_e are similar in EDE images for the two phantoms, whereas the image contrast and CNR_e were lower in the ARFI images of the phantom with a deeper inclusion (phantom 2). Stiffness contrast (Varghese and Ophir 1997), which denotes the ratio of the strain of the background to that of the target, is a widely used metric for evaluating the contrast achieved with ultrasound elastography. However, for the analysis in this study, we only had access to the final ARFI image without the strain distribution from the Siemens Acuson S2000 system. We therefore used the image contrast as defined in eqn (1), to prevent the denominator from becoming too small and introducing numerical instability. Image processing to enhance the image contrast for the EDE strain images was not performed in this study.

The delineation rate obtained with EDE was significantly higher in the clinical studies compared with that for ARFI. One important factor is that the displacement of local tissue perturbed with EDE occurs with larger amplitudes in the millimeter range, compared with the amplitude of ARFI deformation in the range of submillimeters (Nightingale et al. 2001). Insufficient displacement of local tissue with ARFI is due mainly to the increased attenuation incurred by the push beams for larger depths (Correa-Gallego et al. 2014). The relatively

Table 2. Patient imaging results with both EDE and ARFI by the first observer

			Method used to delineate ablated region	
Tumor depth (cm)	No. of patients	Partially visualized on ARFI	ARFI	EDE
<5	15	6/15 (40%)	2/15 (13.3%)	15/15 (100%)
>5 but <10	25	6/25 (24%)	0/25	21/25 (84%)
>10	9	1/9 (11.1%)	0/9	9/9 (100%)
Total	49	13/49 (26.5%)	2/49 (4.1%)	45/49 (91.8%)

Table 3. Patient imaging results with both EDE and ARFI by the second observer

Tumor depth (cm)	No. of patients	Partially visualized with ARFI	Method used to delineate ablated region	
			ARFI	EDE
<5	15	12/15 (80%)	4/15 (26.7%)	9/15 (60%)
>5, but <10	25	13/25 (52%)	1/25 (4%)	19/25 (76%)
>10	9	2/9 (22.2%)	1/9 (11.1%)	6/9 (66.7%)
Total	49	27/49 (55.1%)	6/49 (12.2%)	34/49 (69.4%)

deep location of the ablation zone, the presence of cirrhotic livers and the gas bubbles generated by the ablation procedure contribute to the high attenuation incurred by the push beams (Correa-Gallego et al. 2014). The delineable ablated regions in ARFI images in this study were within 5 cm, which is consistent with previous *ex vivo* (Bing et al. 2011; Nightingale et al. 2001) and *in vivo* (Mariani et al. 2014) studies. For ARFI monitoring of MWA procedures in the study, the ablation zone was stabilized by the antenna. Because the displacement of local tissue is caused by external pushing beams with ARFI, the amplitude of the displacement may have been further suppressed. Although the numbers of delineable cases from the two observers differed for EDE and ARFI, note that both observers indicated that a significant number of delineable cases were obtained with EDE.

The ARFI technique reported in this article was based on utilization of the commercial software, Virtual Touch, on the Siemens Acuson S2000 system. Although ARFI was initially developed for superficial and small masses such as early-stage breast cancer (Nightingale et al. 2001), methods to improve the monitoring ability of thermal ablation for larger masses and deeper locations have been reported (Fahey et al. 2008). In the Fahey et al. study, ARFI was processed off-line with sophisticated tracking algorithms and filters for monitoring RFA procedures. Time-gain control was also applied to compensate for the varying radiation force magnitude caused by attenuation and focal effects (Fahey et al. 2008). The tumor depth for the six patients in the Fahey et al. study was mostly in the range 5–6 cm. Delineable boundaries were achieved for most of the six patients. Performance of ARFI with improved techniques at deeper locations and application to MWA requires further investigation.

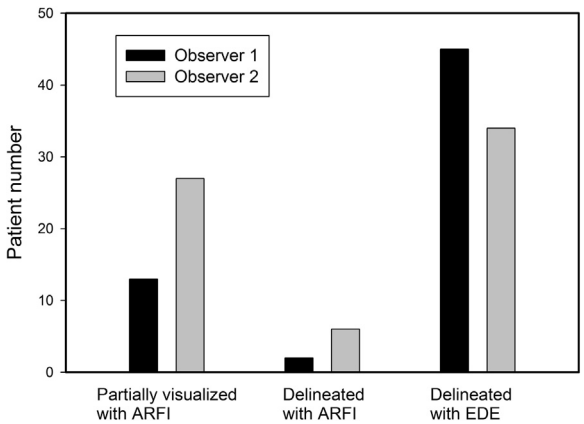

Fig. 6. Number of patient ablated regions delineated with electrode displacement elastography (EDE) and acoustic radiation force impulse (ARFI), respectively, along with the number of ablated regions partially visualized in conjunction with B-mode and ARFI imaging. There were 12 and 2 ablated regions partially visualized and delineable with ARFI imaging, respectively, from observer 1. The corresponding results from observer 2 were 27 and 6, respectively. The numbers of ablation regions delineable with EDE images were 45 and 34, respectively, from observer 1 and 2.

In addition to the ARFI processing techniques discussed above, techniques enhancing the perturbation amplitude might also be helpful in improving the performance of ARFI for monitoring thermal ablation. In the study by Sarvazyan et al. (1998), an optimized waveform for the push beams was simulated to form a sawtooth wave in the focal zone to enhance the spatial energy density delivered to the local tissue. The generation of this optimal waveform is depth dependent and varies for each patient. U.S. Food and Drug Administration standards for clinical ultrasound output constitute another limiting factor for the intensity of the push beam with ARFI, although the standards might be conservative for the short bursts of push beams used (Nightingale et al. 2001).

The rate of delineation of ablation regions with EDE was less dependent on imaging depth because the deformation of local tissue is delivered to the center of the ablation zone by the ablation needle. With less limitation on the perturbation amplitude, processing for EDE could be performed using a relatively compact 2-D cross-correlation-based algorithm. The processing time for EDE was about 2 min on an Intel Core 2 desktop using MATLAB (The MathWorks, Natick, MA, USA), with the pre- and post-compression frames selected by an experienced operator. An algorithm for automatic selection of the pre- and post-compression frames will be implemented as part of future work. For clinical monitoring, real-time feedback to the clinician is essential and could significantly improve strain image quality. Because no

specific parameter optimizations are needed for different patients with EDE, the computational time could be significantly improved with faster software implementation on commercial systems for real-time imaging.

Based on the TM phantom and patient studies reported here, EDE and ARFI were compared with respect to their imaging performance in monitoring MWA. Because of the limited number of delineable ablation regions in ARFI images, the patient study was designed as a binary evaluation. A quantitative analysis of EDE and B-mode image assessments was performed in our previous study (Yang et al. 2016). The performance of the commercial ARFI software, Virtual Touch imaging, could be improved with more advanced processing techniques or advanced push beam profile design, as discussed above. However, the overall ability of ARFI in monitoring MWA is limited by the relatively small perturbation amplitudes produced with radiation force, the increased attenuation in cirrhotic livers and the larger depth range needed for ablation procedures. EDE, with its advantage of not being significantly dependent on tumor depth, stable perturbation amplitudes at all depths and relatively straightforward real-time implementation for commercial systems, could be an alternative technique for monitoring minimally invasive MWA during ablation procedures.

Acknowledgments—This study was funded by National Institutes of Health Grant 2 R01 CA112192. We are grateful to Siemens Medical Solutions USA, Inc., for providing the S2000 Axius Direct Ultrasound Research Interface (URI) and Software licenses. We also sincerely appreciate the support of every clinician and sonographer involved in this study.

REFERENCES

Bharat S, Varghese T. Contrast-transfer improvement for electrode displacement elastography. Phys Med Biol 2006;51:6403–6418.

Bharat S, Techavipoo U, Kiss MZ, Liu W, Varghese T. Monitoring stiffness changes in lesions after radiofrequency ablation at different temperatures and durations of ablation. Ultrasound Med Biol 2005;31:415–422.

Bharat S, Fisher TG, Varghese T, Hall TJ, Jiang J, Madsen EL, Zagzebski JA, Lee FT Jr. Three-dimensional electrode displacement elastography using the Siemens C7 F2 fourSight four-dimensional ultrasound transducer. Ultrasound Med Biol 2008a;34:1307–1316.

Bharat S, Varghese T, Madsen EL, Zagzebski JA. Radio-frequency ablation electrode displacement elastography: A phantom study. Med Phys 2008b;35:2432–2442.

Bing KF, Rouze NC, Palmeri ML, Rotemberg VM, Nightingale KR. Combined ultrasonic thermal ablation with interleaved ARFI image monitoring using a single diagnostic curvilinear array: A feasibility study. Ultrason Imaging 2011;33:217–232.

Chen L, Treece GM, Lindop JE, Gee AH, Prager RW. A quality-guided displacement tracking algorithm for ultrasonic elasticity imaging. Med Image Anal 2009;13:286–296.

Correa-Gallego C, Karkar AM, Monette S, Ezell PC, Jarnagin WR, Kingham TP. Intraoperative ultrasound and tissue elastography measurements do not predict the size of hepatic microwave ablations. Acad Radiol 2014;21:72–78.

Fahey BJ, Nelson RC, Hsu SJ, Bradway DP, Dumont DM, Trahey GE. In vivo guidance and assessment of liver radio-frequency ablation with acoustic radiation force elastography. Ultrasound Med Biol 2008;34:1590–1603.

Harari CM, Magagna M, Bedoya M, Lee FT Jr, Lubner MG, Hinshaw JL, Ziemlewicz T, Brace CL. Microwave ablation: Comparison of simultaneous and sequential activation of multiple antennas in liver model systems. Radiology 2016;278:95–103.

Ingle A, Varghese T. Three-dimensional sheaf of ultrasound planes reconstruction (SOUPR) of ablated volumes. IEEE Trans Med Imaging 2014;33:1677–1688.

Jiang J, Brace C, Andreano A, DeWall RJ, Rubert N, Fisher TG, Varghese T, Lee F Jr, Hall TJ. Ultrasound-based relative elastic modulus imaging for visualizing thermal ablation zones in a porcine model. Phys Med Biol 2010;55:2281–2306.

Lencioni R, Crocetti L. Local-regional treatment of hepatocellular carcinoma. Radiology 2012;262:43–58.

Liang P, Wang Y. Microwave ablation of hepatocellular carcinoma. Oncology 2007;72(Suppl 1):124–131.

Lubner MG, Brace CL, Ziemlewicz TJ, Hinshaw JL, Lee FT Jr. Microwave ablation of hepatic malignancy. Semin Interv Radiol 2013;30:56–66.

Maluccio M, Covey A. Recent progress in understanding, diagnosing, and treating hepatocellular carcinoma. CA Cancer J Clin 2012;62:394–399.

Mariani A, Kwiecinski W, Pernot Balvay D, Tanter M, Clement O, Cuenod CA, Zinzindohoue F. Real time shear waves elastography monitoring of thermal ablation: In vivo evaluation in pig livers. J Surg Res 2014;188:37–43.

Murakami R, Yoshimatsu S, Yamashita Y, Matsukawa T, Takahashi M, Sagara K. Treatment of hepatocellular carcinoma: Value of percutaneous microwave coagulation. AJR Am J Roentgenol 1995;164:1159–1164.

Nightingale KR, Palmeri ML, Nightingale RW, Trahey GE. On the feasibility of remote palpation using acoustic radiation force. J Acoust Soc Am 2001;110:625–634.

Ophir J, Cespedes I, Ponnekanti H, Yazdi Y, Li X. Elastography: A quantitative method for imaging the elasticity of biological tissues. Ultrasonic imaging 1991;13:111–134.

Pareek G, Wilkinson ER, Bharat S, Varghese T, Laeseke PF, Lee FT Jr, Warner TF, Zagzebski JA, Nakada SY. Elastographic measurements of in-vivo radiofrequency ablation lesions of the kidney. J Endourol 2006;20:959–964.

Qian GJ, Wang N, Shen Q, Sheng YH, Zhao JQ, Kuang M, Liu GJ, Wu MC. Efficacy of microwave versus radiofrequency ablation for treatment of small hepatocellular carcinoma: Experimental and clinical studies. Eur Radiol 2012;22:1983–1990.

Rubert N, Bharat S, DeWall RJ, Andreano A, Brace C, Jiang J, Sampson L, Varghese T. Electrode displacement strain imaging of thermally-ablated liver tissue in an in vivo animal model. Med Phys 2010;37:1075–1082.

Sarvazyan AP, Rudenko OV, Swanson SD, Fowlkes JB, Emelianov SY. Shear wave elasticity imaging: A new ultrasonic technology of medical diagnostics. Ultrasound Med Biol 1998;24:1419–1435.

Shiina S, Tateishi R, Arano T, Uchino K, Enooku K, Nakagawa H, Asaoka Y, Sato T, Masuzaki R, Kondo Y, Goto T, Yoshida H, Omata M, Koike K. Radiofrequency ablation for hepatocellular carcinoma: 10-Year outcome and prognostic factors. Am J Gastroenterol 2012;107:569–577. quiz 578.

Thamtorawat S, Hicks RM, Yu J, Siripongsakun S, Lin WC, Raman SS, McWilliams JP, Douek M, Bahrami S, Lu DS. Preliminary outcome of microwave ablation of hepatocellular carcinoma: Breaking the 3-cm barrier? J Vasc Interv Radiol 2016;27:623–630.

Van Vledder MG, Boctor EM, Assumpcao LR, Rivaz H, Foroughi P, Hager GD, Hamper UM, Pawlik TM, Choti MA. Intra-operative ultrasound elasticity imaging for monitoring of hepatic tumour thermal ablation. HPB (Oxford) 2010;12:717–723.

Varghese T. Quasi-static ultrasound elastography. Ultrasound Clin 2009;4:323–338.

Varghese T, Ophir J. A theoretical framework for performance characterization of elastography: The strain filter. IEEE Trans Ultrason Ferroelectr Freq Control 1997;44:164–172.

Varghese T, Shi H. Elastographic imaging of thermal lesions in liver in-vivo using diaphragmatic stimuli. Ultrason Imaging 2004;26: 18–28.

Varghese T, Zagzebski JA, Lee FT Jr. Elastographic imaging of thermal lesions in the liver in vivo following radiofrequency ablation: Preliminary results. Ultrasound Med Biol 2002;28:1467–1473.

Varghese T, Techavipoo U, Liu W, Zagzebski JA, Chen Q, Frank G, Lee FT Jr. Elastographic measurement of the area and volume of thermal lesions resulting from radiofrequency ablation: Pathologic correlation. AJR Am J Roentgenol 2003a;181: 701–707.

Varghese T, Zagzebski JA, Rahko P, Breburda CS. Ultrasonic imaging of myocardial strain using cardiac elastography. Ultrason Imaging 2003b;25:1–16.

Varghese T, Techavipoo U, Zagzebski JA, Lee FT Jr. Impact of gas bubbles generated during interstitial ablation on elastographic depiction of in vitro thermal lesions. J Ultrasound Med 2004;23:535–544. quiz 545–546.

Wells SA, Hinshaw JL, Lubner MG, Ziemlewicz TJ, Brace CL, Lee FT Jr. Liver ablation: Best practice. Radiol Clin North Am 2015;53:933–971.

Yang W, Ziemlewicz TJ, Varghese T, Alexander ML, Rubert N, Ingle AN, Lubner MG, Hinshaw JL, Wells SA, Lee FT. Post-procedure evaluation of microwave ablations of hepatocellular carcinomas using electrode displacement elastography. Ultrasound Med Biol 2016;42:2893–2902.

Zhou Z, Wu W, Wu S, Xia J, Wang CY, Yang C, Lin CC, Tsui PH. A survey of ultrasound elastography approaches to percutaneous ablation monitoring. Proc Inst Mech Eng H 2014;228:1069–1082.

Ziemlewicz TJ, Hinshaw JL, Lubner MG, Brace CL, Alexander ML, Agarwal P, Lee FT Jr. Percutaneous microwave ablation of hepatocellular carcinoma with a gas-cooled system: Initial clinical results with 107 tumors. J Vasc Interv Radiol 2015;26:62–68.

Ziemlewicz TJ, Wells SA, Lubner MG, Brace CL, Lee FT Jr, Hinshaw JL. Hepatic tumor ablation. Surg Clin North Am 2016; 96:315–339.